PCCP

PAPER

Cite this: *Phys. Chem. Chem. Phys.*, 2015, **17**, 8006

Specific features of electronic structures and optical susceptibilities of g-BC_3 and t-BC_3 phases

A. H. Reshak[ab]

Received 18th January 2015,
Accepted 17th February 2015

DOI: 10.1039/c5cp00318k

www.rsc.org/pccp

Details of comparison for some specific features of electronic structures and optical susceptibilities of g-BC_3 and t-BC_3 phases are provided. Calculations show that the g-BC_3 phase is a narrow band gap semiconductor constructed from the ABAB stacking sequence. Whereas t-BC_3 is a metallic phase constructed by a sandwich-like metal–insulator lattice from an alternately stacking sequence of metallic CBC and insulating CCC blocks. The two phases possess only two types of bonds (B–C and C–C). The density of states at the Fermi level $N(E_F)$ of the t-BC_3 phase is determined by the overlapping of B-2p and C-2p empty orbitals of the CBC block with C-2p empty orbitals of the CCC block, and the shape of the Fermi surface originated from these empty orbitals. The B atoms cause a small perturbation on the C-ring's structure and hence to the charge density distribution. The linear optical properties of the two phases confirm the existence of the lossless regions and the considerable anisotropy. The second harmonic generation of the t-BC_3 phase shows that $\chi^{(2)}_{123}(\omega)$ is the dominant component of about 3.9 pm V^{-1} at the static limit and 5.8 pm V^{-1} at λ = 1064 nm, which suggests that the t-BC_3 phase could be considered as a promising nonlinear optical material in comparison with the well known $KTiOPO_4$ nonlinear optical single crystal.

1. Introduction

In recent years there has been great interest in boron-rich diamond materials due to their excellent chemical and physical properties.[1–8] It has been found that these materials possess high mechanical strength, high hardness, high thermal conductivity, high electron and hole mobility, high chemical inertness, and low mass density.[9,10] Ekimov *et al.*[1] reported that superconductivity was found in boron-doped diamond synthesized at high temperature and high pressure. Increasing the dopant concentrations led to the enhancement of superconductivity.[11–13] These superhard materials are of great demand for numerous applications for instance in the electronic industry, solar cell production and mechanical machining. Several researchers focus their attention on finding novel superhard materials with good conductivity.[14,15] Combining superhard and metallic properties is of great interest for the creation of multifunctional materials with potential applications as metal–insulator junctions, metal–insulator devices and photonic devices.[16] Recently Ali *et al.*[17] studied superconductivity in the diamond-like BC_3 phase using the pseudopotential density functional method (DFT) within the generalized gradient approximation (GGA). They found that the t-BC_3 phase is stable with space group $P\bar{4}2m$, and exhibits metallic behavior at ambient and high pressures. While g-BC_3 is a semiconductor at both ambient and high pressures. Liu *et al.*[18] by using the first principles calculations predicted that the superhard t-BC_3 phase originated from the cubic diamond structure. It has been found that the t-BC_3 phase is constructed by a sandwich-like metal–insulator lattice from an alternately stacking sequence of metallic CBC and insulating CCC blocks along the *c*-axis. They predicted the synthesis of the t-BC_3 phase from the g-BC_3 phase at high pressure. Also they confirmed the stability of both phases at the space group $P\bar{4}2m$ and *Cmcm*, respectively. A diamond-like d-BC_3 phase has been synthesized from g-BC_3 at high pressure and temperature, the phase transition from the g-BC_3 to d-BC_3 phase was confirmed by the analysis of Raman scattering data.[19] Tomanek[20] determined the equilibrium geometry and electronic structure of BC_3 by using the *ab initio* pseudopotential local orbital approach within local density approximation. It has been reported that BC_3 is a layered material with graphitic structure. Liu *et al.*[9] have explored the crystal structures of synthesized diamond-like d-BC_3 using the particle swarm optimization algorithm combined with first-principles structural optimizations. They uncovered three intriguing metallic low-energy structures, the first is orthorhombic *Pmma* which consists of a sandwich-like "Blayer" between C layers, the second structure is orthorhombic *Pmma* with novel B–B bonding

[a] *New Technologies – Research Centre, University of West Bohemia, Univerzitni 8, 306 14 Pilsen, Czech Republic. E-mail: maalidph@yahoo.co.uk; Tel: +420 777729583*

[b] *Center of Excellence Geopolymer and Green Technology, School of Material Engineering, University Malaysia Perlis, 01007 Kangar, Perlis, Malaysia*

and the third one is tetragonal $P\bar{4}m2$. The calculations show that the three phases are superhard and superconducting materials. Sun *et al.*[21] have investigated different staking arrangements of the g-BC_3 using the *ab initio* pseudopotential DFT method at an equilibrium of zero pressure. They reported that only two possible structures were found, these are ABAB,..., and ABCABC,..., stacking sequences. Lei Li *et al.*[22] have calculated the optical properties of t-BC_3 by using the pseudopotential DFT method within GGA. They reported that t-BC_3 is an optical anisotropic phase and its electron-deficiency characteristic can cause some features in the low energy region.

From above, it is clear that the previous experimental and theoretical work is devoted to the synthesis of BC_3, study of the crystal structure, electronic properties, elastic properties with very few reports on the linear optical properties, all the previous calculations are done using non-full potential methods. Therefore, due to a lack of information regarding the electronic charge density distribution, Fermi surface and the linear and nonlinear optical properties for the superhard metallic g-BC_3 and t-BC_3 compounds, we performed comprehensive theoretical calculations based on the density functional theory (DFT) within all-electron full potential method. The calculations are performed using three types of exchange correlation potentials within the full potential method to ascertain the effect of exchange correlation on the electronic structure and hence the linear and nonlinear optical properties. In this calculation we have employed the state-of-the-art all-electron full potential linear augmented plane wave (FPLAPW) method which has been proven to be one of the most accurate methods

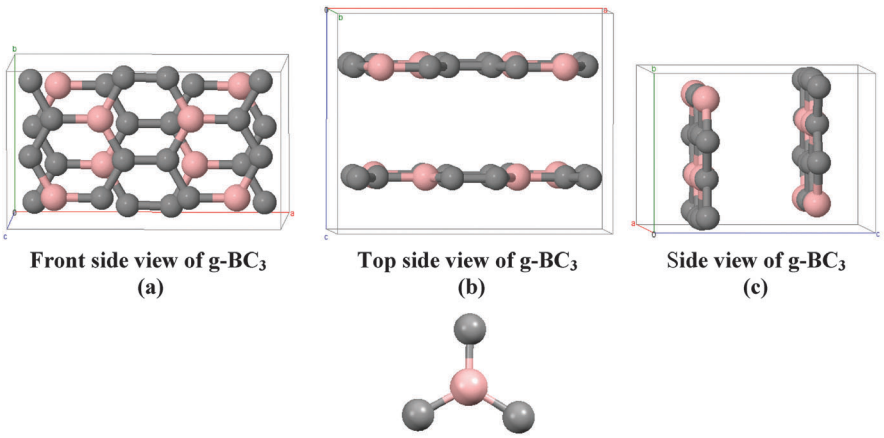

Fig. 1 Fragment of the crystal structure of the g-BC_3 phase which has ABAB,..., stacking sequence; (a) front side view of g-BC_3; (b) top side view of g-BC_3; (c) side view of g-BC_3; (d) asymmetric unit of g-BC_3, where C atom appears in gray color and B atom in pink color.

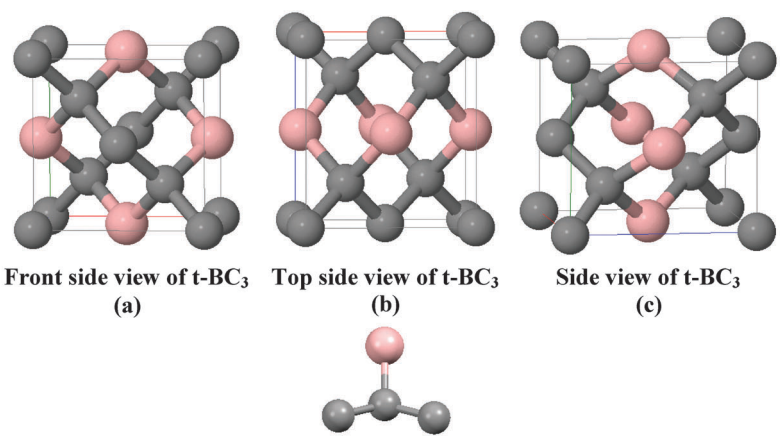

Fig. 2 Fragment of the crystal structure of the t-BC_3 phase which is constructed by two different building blocks, these are CCC (composed of two C sheets) and CBC (composed of one B sheet and one C sheet). These building blocks form sandwich-like layered structure with alternately stacking sequences of atomic planes C–C–B–C–C–C–B–C–C (a sandwich-like conducting super-hard boron carbide); (a) front side view of t-BC_3; (b) top side view of t-BC_3; (c) side view of t-BC_3; (d) asymmetric unit of t-BC_3, where C atom appears in gray color and B atom in pink color.

for the computation of the electronic structure of solids within DFT.[23–26]

2. Details of calculations

The graphitic-like g-BC_3 crystallizes in orthorhombic space group *Cmcm*, with the ABAB,. . ., stacking sequence as illustrated in Fig. 1(a–d). In the unit cell of g-BC_3 the structural parameters are a = 8.834 Å, b = 5.104 Å and c = 7.071 Å, the B atom is located at (0.167, 0.823, 0.25), C1 at (0.159, 0.323, 0.25), C2 at (0.792, 0.562, 0.25) and C3 at (0.421, 0.585, 0.25). The boron-rich diamond t-BC_3 crystallizes in tetragonal space group $P\bar{4}2m$ with eight atoms per unit cell as illustrated in Fig. 2(a–d). The structural parameters of t-BC_3 are $a = b$ = 3.513 Å and c = 3.871 Å, the B atom is situated at (0.5 0.0 0.5), C1 at (0.0 0.0 0.0), C2 at (0.25 0.25 0.229) and C3 at (0.5 0.5 0.0). In both (t-BC_3 and g-BC_3) phases the B atom connected to three C atoms in different configurations as shown in Fig. 1(d) and 2(d).

Using the state-of-the-art all-electron full potential linear augmented plane wave (FPLAPW) method as implemented in WIEN2k code[27] within generalized gradient approximation (PBE-GGA),[28] the geometry of t-BC_3 and g-BC_3 is relaxed by minimizing the forces acting on each atom. The structures are totally relaxed when the forces on each atom reach values less than 1 mRy a.u^{-1}. From the relaxed geometry the ground state properties of t-BC_3 and g-BC_3 are calculated within the local density approximation (CA-LDA),[29] PBE-GGA and Engel–Vosko generalized gradient approximation (EVGGA).[30] To overcome the DFT-LDA/GGA band gap's underestimation we have introduced EVGGA. It is well known that EVGGA is able to reproduce better exchange potential at the expense of less agreement in the exchange energy. This approach yields better band splitting compared to LDA and GGA. The plane-wave cuttoff is defined by the product of the smallest atomic sphere radius times the magnitude of the largest reciprocal-lattice vector ($R_{MT} \times K_{MAX}$) which is taken to be equal to 8. In the muffin-tin (MT) spheres the potential and charge density are expanded in spherical harmonics with l_{max} = 8 and nonspherical components up to l_{max} = 6. In the interstitial region the potential and the charge density are represented by Fourier series. Self-consistency is obtained using 400 $\vec{k}$ points in the irreducible Brillouin zone (IBZ). The self-consistent calculations are converged since the total energy of the system is stable within 0.00001 Ry. The electronic band structure, density of states, electronic charge density distribution, Fermi surface and the linear optical properties are calculated within 600 $\vec{k}$ points in the IBZ, the nonlinear optical properties of t-BC_3 are calculated within 1200 $\vec{k}$ points in the IBZ.

3. Results and discussion

3.1. Electronic band structure, density of states and the electronic charge density

The electronic band structure dispersion of g-BC_3 and t-BC_3 phases is constructed using three different types of exchange correlation potential (XC) to ascertain the effect of XC on the band dispersion. These are LDA, GGA and EVGGA which show there is significant enhancement in the band gap's value of g-BC_3 when one moves from LDA → GGA → EVGGA, to be 0.3 eV (LDA), 0.4 eV (GGA) and 0.7 (EVGGA). Calculations show that EVGGA exhibits better results in comparison to LDA and GGA, since EVGGA brings the calculated energy gap of g-BC_3 (0.7 eV) in agreement with previous results (0.66 eV) using LDA.[31]

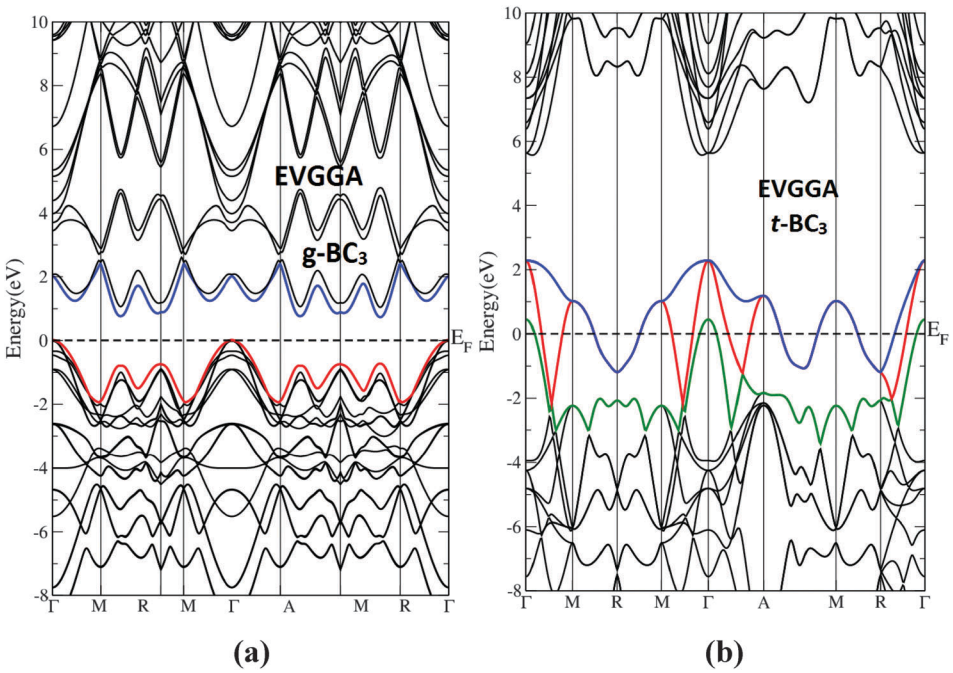

Fig. 3 The calculated electronic band structure of (a) the g-BC_3 phase using EVGGA; and (b) the t-BC_3 phase using EVGGA.

Whereas for the t-BC_3 phase moving LDA → GGA → EVGGA exhibits small influences on the dispersions of the electronic band structure. Therefore, we selected to show the electronic band structure of g-BC_3 and t-BC_3 phases obtained by EVGGA. Fig. 3(a) illustrates the electronic band structure of g-BC_3 which confirm the semiconducting nature of this phase. The valence band maximum (VBM) is situated at the center of BZ while the conduction band minimum (CBM) is located in the mid way between *M* and *R* points of BZ, resulting in an indirect energy gap. The Fermi level (E_F) is situated at 0.0 eV. Fig. 3(b) shows the electronic band structure of the t-BC_3 phase which illustrated that there are three bands cuts E_F to form the shape of the Fermi surface. Calculations show that the top of the valence band is about 2.4 eV above E_F in reasonable agreement with previous results (2.28 eV (ref. 17) and 2.7 eV (ref. 18)). Therefore the t-BC_3 phase which is derived from the g-BC_3 phase has metallic nature.

To investigate the contribution of -s/-p orbitals of each atom and the hybridizations between these orbitals the total and the angular momentum resolved projected density of states for g-BC_3 and t-BC_3 phases are calculated and represented in Fig. 4(a and b), 5(a–c) and 6(a–c). In Fig. 4(a) and (b) we demonstrate the influences of replacing the exchange correlations

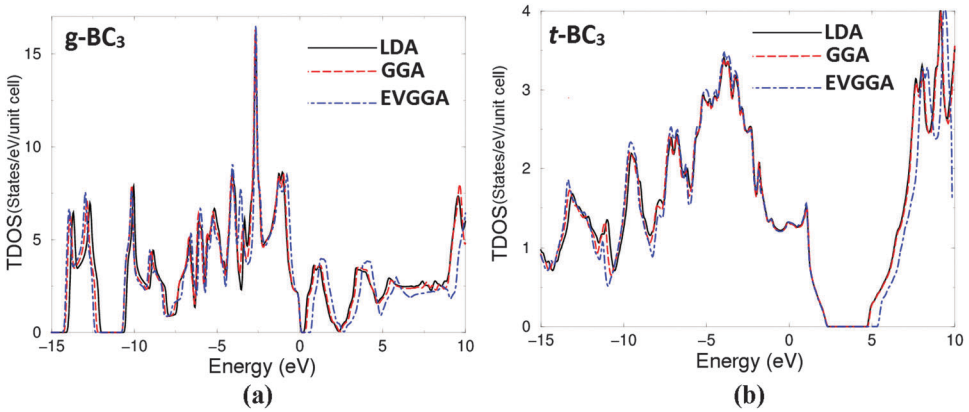

Fig. 4 Calculated total density of states (states/eV per unit cell) using LDA, GGA and EVGGA; (a) g-BC_3 phase; (b) t-BC_3 phase.

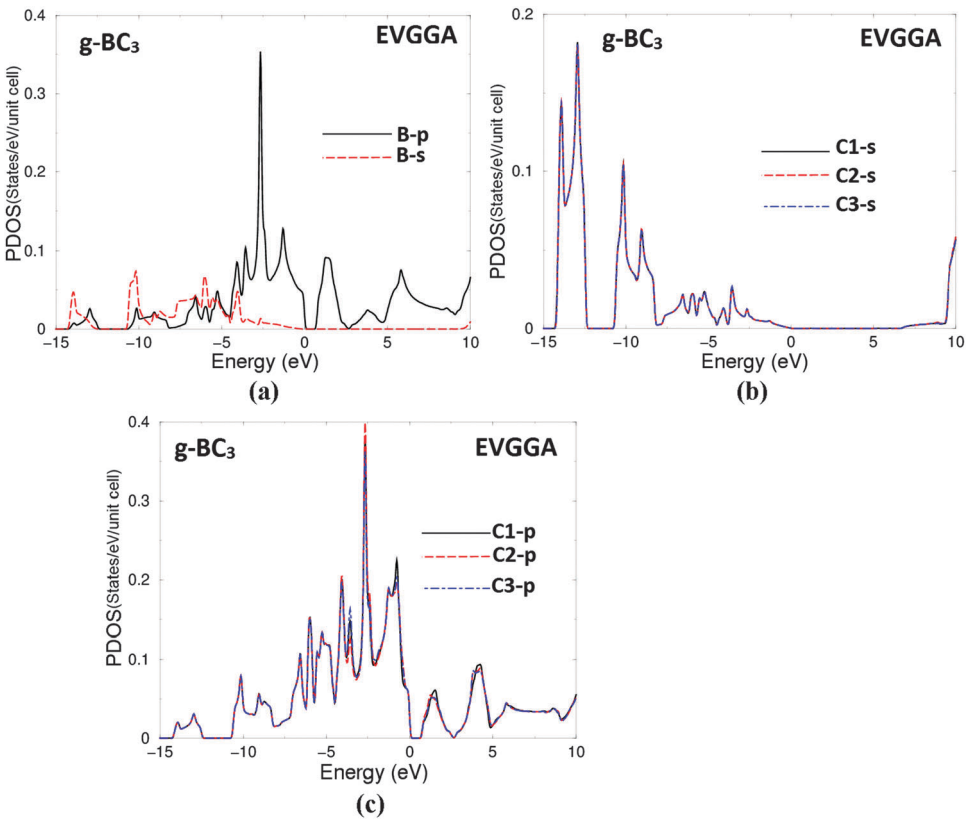

Fig. 5 (a)–(c) Calculated partial density of states (states/eV per unit cell) B-s/p and C-s/p for g-BC_3 phase using EVGGA.

potentials (LDA → GGA → EVGGA) on the total density of states. For g-BC_3 it is clear that the structure below −12.0 eV shifts towards lower energies whereas the structures from the CBM and above move towards higher energies when one moves from LDA → GGA → EVGGA. For the t-BC_3 phase the structure below −10.0 eV shifts towards lower energies whereas the structures from 5.0 eV and above shifts towards higher energies when we replace LDA by GGA and GGA by EVGGA. It is clear that EVGGA yields better band splitting than LDA and GGA and hence overcomes the band gap's underestimation caused by LDA and GGA. Therefore, we show the calculated angular momentum resolved projected density of states by using EVGGA. Fig. 5(a–c) illustrates the contribution of B-s/p and C1,2,3-s/p states in the g-BC_3 phase, it is clear that the B-p and C1,2,3-s/p states contribute along the whole energy scale while the B-s state contributes only below E_F. There exists a strong hybridization between B-p and C1,2,3-p states in the energy range extended from −5.0 eV up to CBM. In the energy region between −14.0 and −12.0 eV, the B-s/p states hybridize with C1,2,3-p states. At around −10.0 eV, the C1,2,3-p states hybridized with the B-s state and also with C1,2,3-s states. It is clear that all C1,2,3-s/p states show the same contribution due to the fact that g-BC_3 has the ABAB,. . ., stacking sequence.

Fig. 6(a–c) shows B-s/p and C1,2,3-s/p partial density of states for the t-BC_3 phase, it has been found that the C2-s/p states show different contributions than that of C1,3-s/p states, which is attributed to the fact that the t-BC_3 phase is constructed by two different building blocks, these are CCC (composed of two C sheets) and CBC (composed of one B sheet and one C sheet), therefore C1 and C3 belong to the CCC block, while C2 belongs to the CBC block. These building blocks form sandwich-like layered structure with alternately stacking sequences of atomic planes C–C–B–C–C–C–B–C–C (a sandwich-like conducting super-hard boron carbide) as illustrated in Fig. 2. There exists a strong hybridization between B-s and C1,3-s states at around −12.0 eV. The B-p state hybridized with C1,2,3-s/p states in the energy range between 5.0 up to 10.0 eV. The strong hybridization may lead to covalent bonding.

The density of states at the Fermi level $N(E_F)$ is determined by the overlapping of B-2p and C-2p empty orbitals of the CBC block and C-2p empty orbitals of the CCC block. This overlapping is strong enough to indicate the metallic nature of the t-BC_3 phase. We have calculated the values of $N(E_F)$ for the total and partial density of states using LDA, GGA and EVGGA. The electronic specific heat coefficient (γ) can be obtained using the expression $\gamma = \frac{1}{3}\pi^2 N(E_F) k_B{}^2$, where k_B is the Boltzmann constant. The calculated $N(E_F)$ and (γ) for the total and partial density of states are listed in Table 1, which shows the obtained values of $N(E_F)$ and (γ) using LDA > GGA > EVGGA.

To investigate the bonding characters we have calculated the electronic charge density distribution for the two phases g-BC_3 and t-BC_3 in (001) and (101) crystallographic planes. Fig. 7(a) and (b) illustrates (001) and (101) crystallographic planes of the g-BC_3 phase which shows the ABAB,. . ., stacking sequence and the two types of bonds (B–C and C–C). Due to the electro-negativity

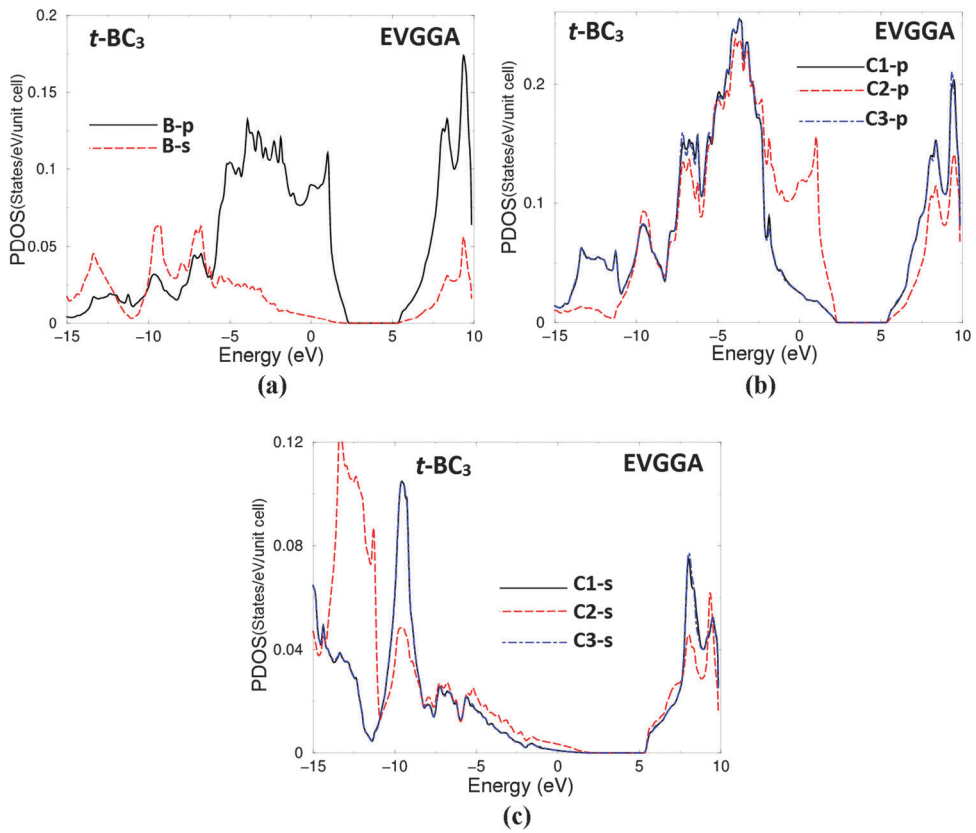

Fig. 6 (a)–(c) Calculated partial density of states (states/eV per unit cell) B-s/p and C-s/p for t-BC_3 phase using EVGGA.

Table 1 Calculated density of states at Fermi level $N(E_F)$ in (states/Ry per cell) for t-BC_3, B-s/p and C1,2,3-s/p states along with the calculated electronic specific heat coefficient (γ) in (mJ mol^{-1} K^2)

$N(E_F)$	LDA	GGA	EVGGA
$N(E_F)$@t-BC_3	18.05	17.90	17.12
$N(E_F)$@B-s	0.06	0.06	0.06
$N(E_F)$@B-p	1.23	1.21	1.20
$N(E_F)$@C1-s	0.01	0.01	0.01
$N(E_F)$@C1-p	0.38	0.37	0.34
$N(E_F)$@C2-s	0.05	0.05	0.05
$N(E_F)$@C2-p	1.61	1.62	1.59
$N(E_F)$@C3-s	0.01	0.01	0.01
$N(E_F)$@C3-p	0.38	0.37	0.34
γ@t-BC_3	3.13	3.12	3.10
γ@B-s	0.01	0.01	0.01
γ@B-p	0.21	0.21	0.21
γ@C1-s	0.00	0.00	0.00
γ@C1-p	0.07	0.06	0.06
γ@C2-s	0.01	0.01	0.01
γ@C2-p	0.28	0.28	0.28
γ@C3-s	0.00	0.00	0.00
γ@C3-p	0.07	0.06	0.06

difference between C (2.55) and B (2.04) atoms, there exists a strong covalent bonding between B–C and C–C. From the electro-negativity difference one can determine the degree of covalency which is a very important factor to estimate the hardness of the materials.[32] The blue (1.0000) color surrounding B and C atoms (Fig. 7) is attributed to the maximum charge accumulation site. It has been found that the B atoms cause a small perturbation on the C-ring's structure and hence to the charge density as it is clear from Fig. 7(a). Following this figure one can see that the charge density distribution in the center of the hexagon in which the two C atoms are substituted by two B atoms is perturbed in comparison to the next pure carbon ring, which is attributed to the covalent radii differences between B (0.85 Å) and C (0.70 Å) atoms and the electro-negativity differences between B and C atoms. This perturbation leads to a slight difference in the bond lengths of B–C bond (1.539 Å) than that of the C–C bond (1.409 Å), these values agree well with the previous calculation 1.55 Å (B–C) and 1.42 Å (C–C).[20] Since the t-BC_3 phase is constructed by two different building blocks, CCC (two C sheets) and CBC (one B sheet and one C sheet), one can see that the (001) plane shows only C atoms while the (101) plane represents all atoms, which confirms our previous findings that the above mentioned building blocks form sandwich-like layered structure with alternately stacking sequences of atomic planes C–C–B–C–C–C–B–C–C. The calculated bond lengths of the t-BC_3 phase for C–C and B–C bonds are 1.523 Å and 1.629 Å, respectively, which agree well with previous calculation 1.522 Å (C–C) and 1.627 Å (B–C).[18]

3.2. Fermi surface

The shape of the Fermi surface of the t-BC_3 phase originates from B-2p and C-2p empty orbitals (which are persistent to sp^3 hybridized B–C bonds) of the CBC block with small contribution of C-2p empty orbitals of the CCC block. Therefore, the metallic nature of the t-BC_3 phase corresponds to the CBC block. The calculated Fermi surface of the t-BC_3 phase is represented in Fig. 8(a–d). Fig. 8(a) and (b) shows B/C-2p empty orbitals of the

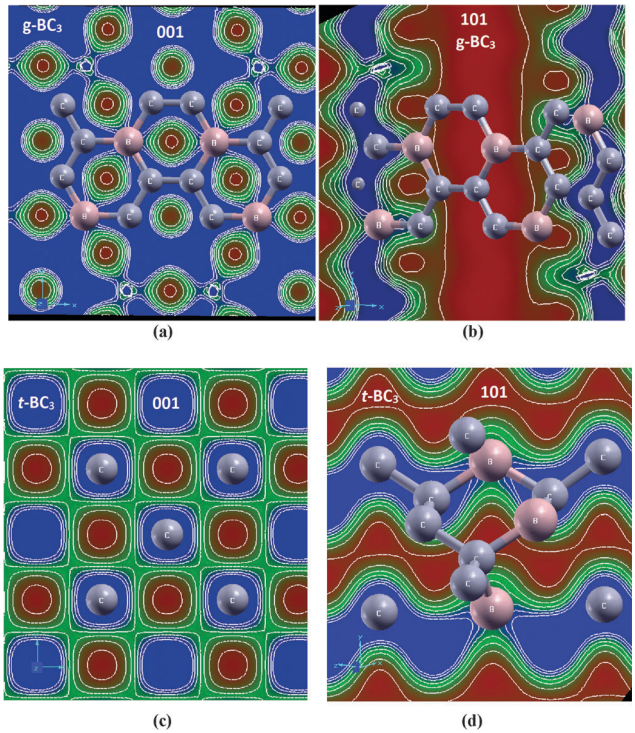

Fig. 7 The calculated electron charge density distribution were calculated for; (a) (001) crystallographic plane of g-BC_3; (b) (101) crystallographic plane of g-BC_3; (c) (001) crystallographic plane of t-BC_3; (d) (101) crystallographic plane of t-BC_3.

CBC block, while Fig. 8(c) represents the small contribution of C-2p empty orbitals of the CCC block. The shape of the Fermi surface is illustrated by Fig. 8(d). The Fermi level is determined *via* the Kohn–Sham eigenvalue of the highest occupied state. The Fermi surface consists of empty areas that represented the holes and shaded areas corresponding to the electrons. The shape of the Fermi surface helps to predict the magnetic, electrical, thermal and optical properties of the metallic and semimetallic materials.

3.3. Linear optical response

In this section we will turn our attention on calculating and comparing the optical properties of g-BC_3 and t-BC_3 phases. As these two phases have different space groups and different characters, we expected to get different optical properties. At first, since the g-BC_3 phase is a semiconductor having an orthorhombic space group *Cmcm*, with the ABAB,…, stacking sequence, this symmetry allows only three tensor components along the polarization directions [100], [010] and [001] with respect to the crystalline axes. These are $\varepsilon^{xx}(\omega)$, $\varepsilon^{yy}(\omega)$ and $\varepsilon^{zz}(\omega)$. The imaginary part of the optical dielectric function's dispersion can be obtained using the following formula;[33,34]

$$\varepsilon_2^{ij}(\omega) = \frac{\omega_P^{ij}\tau}{\omega(1+\omega^2\tau^2)} + \frac{8\pi^2\hbar^2e^2}{m^2V}\sum_k\sum_{cv}(f_c - f_v)\frac{p_{cv}^i(k)p_{vc}^j(k)}{E_{vc}^2}\delta[E_c(k) - E_v(k) - \hbar\omega] \quad (1)$$

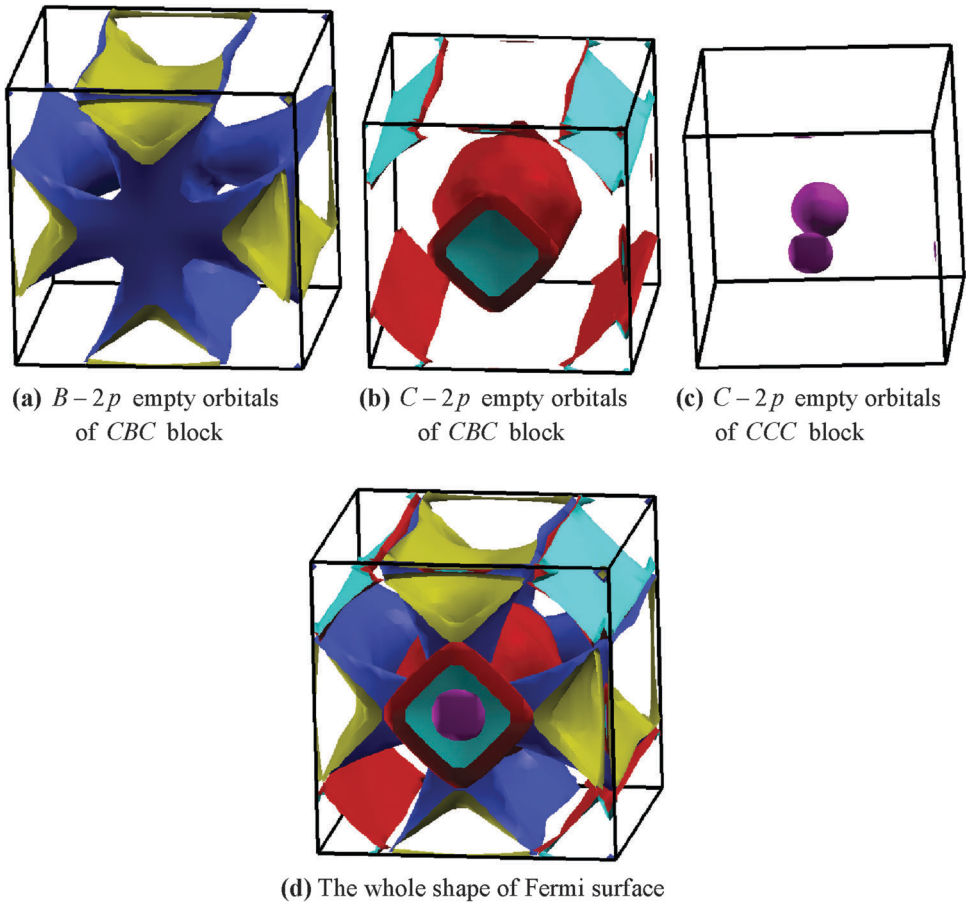

Fig. 8 Calculated Fermi surface for t-BC_3 phase; (a) B-2p empty orbitals of CBC block; (b) C-2p empty orbitals of CBC block; (c) C-2p empty orbitals of CCC block; (d) the whole shape of Fermi surface.

where m, e and $\hbar$ are the electron mass, charge and Planck's constant, respectively. f_c and f_v represent the Fermi distributions of the conduction and valence bands, respectively. The term $p_{cv}^{i}(k)$ denotes the momentum matrix element transition from the energy level c of the conduction band to the level v of the valence band at a certain k-point in the BZ and V is the unit cell volume. τ is the mean free time between collisions and ε_{kn} is $E_n(k) - E_F$.

The t-BC_3 phase is metallic having tetragonal space group $P\bar{4}2m$. For being tetragonal structure therefore, there are only two tensor components $\varepsilon^{xx}(\omega) = \varepsilon^{yy}(\omega)$ and $\varepsilon^{zz}(\omega)$ along the polarization directions [100] and [001], thus t-BC_3 is a uniaxial crystal. For the metallic phase we need to consider the intra-band transition (Drude term) in addition to the inter-band transitions as follows:[33,34]

$$\varepsilon_2^{ij}(\omega) = \varepsilon_{2\text{intra}}^{ij}(\omega) + \varepsilon_{2\text{inter}}^{ij}(\omega) \quad (2)$$

$$\omega_P^{ij\,2} = \frac{8\pi}{3}\sum_{kn} \vartheta_{kn}^{ij\,2}\delta(\varepsilon_{kn}) \quad (3)$$

where ϑ_{kn}^{ij} is the electron velocity and ω_P is the anisotropic plasma frequency.[35] The calculated values of ω_P^{xx} and ω_P^{zz} are listed in Table 2.

Fig. 9(a) shows the spectral structure of $\varepsilon_2(\omega)$ for the g-BC_3 phase, one can see that there is a very sharp strong peak at around 2.0 eV formed by $\varepsilon_2^{xx}(\omega)$ and $\varepsilon_2^{yy}(\omega)$. The weakness of the other structures could be explained by the fact that $\varepsilon_2(\omega)$ scales as $\frac{1}{\omega^2}$. It is very interesting to see that both $\varepsilon_2^{xx}(\omega)$ and $\varepsilon_2^{yy}(\omega)$ are isotropic along the whole energy scale, whereas $\varepsilon_2^{zz}(\omega)$ exhibits a strong anisotropy with both $\varepsilon_2^{xx}(\omega)$ and $\varepsilon_2^{yy}(\omega)$. The optical absorption's edge occurs at around 0.5 eV, which gives the threshold for the optical transitions between the top of the valence band and the bottom of the conduction band (B-s/p, C1,2,3-p). The strong high peak is due to the optical transitions between B-s/p and C1,2,3-s/p states. The last structure is due to the electric-dipole transitions between B-s/p and C1,2,4-s/p of the VBs to B-p and C1,2,3-p of the CB. From the existence information about the imaginary part of the optical dielectric functions one can derive the real part using Kramers–Kronig relations.[34] The three components of the real part $\varepsilon_1^{xx}(\omega)$, $\varepsilon_1^{yy}(\omega)$

Table 2 The calculated ω_P^{xx} and ω_P^{zz} of t-BC_3 phases when $\varepsilon_1^{xx}(\omega)$ and $\varepsilon_1^{zz}(\omega)$ crosses zero

xc	ω_P^{xx}	ω_P^{zz}
LDA	7.352	4.510
GGA	7.409	4.482
ECGGA	7.383	4.269

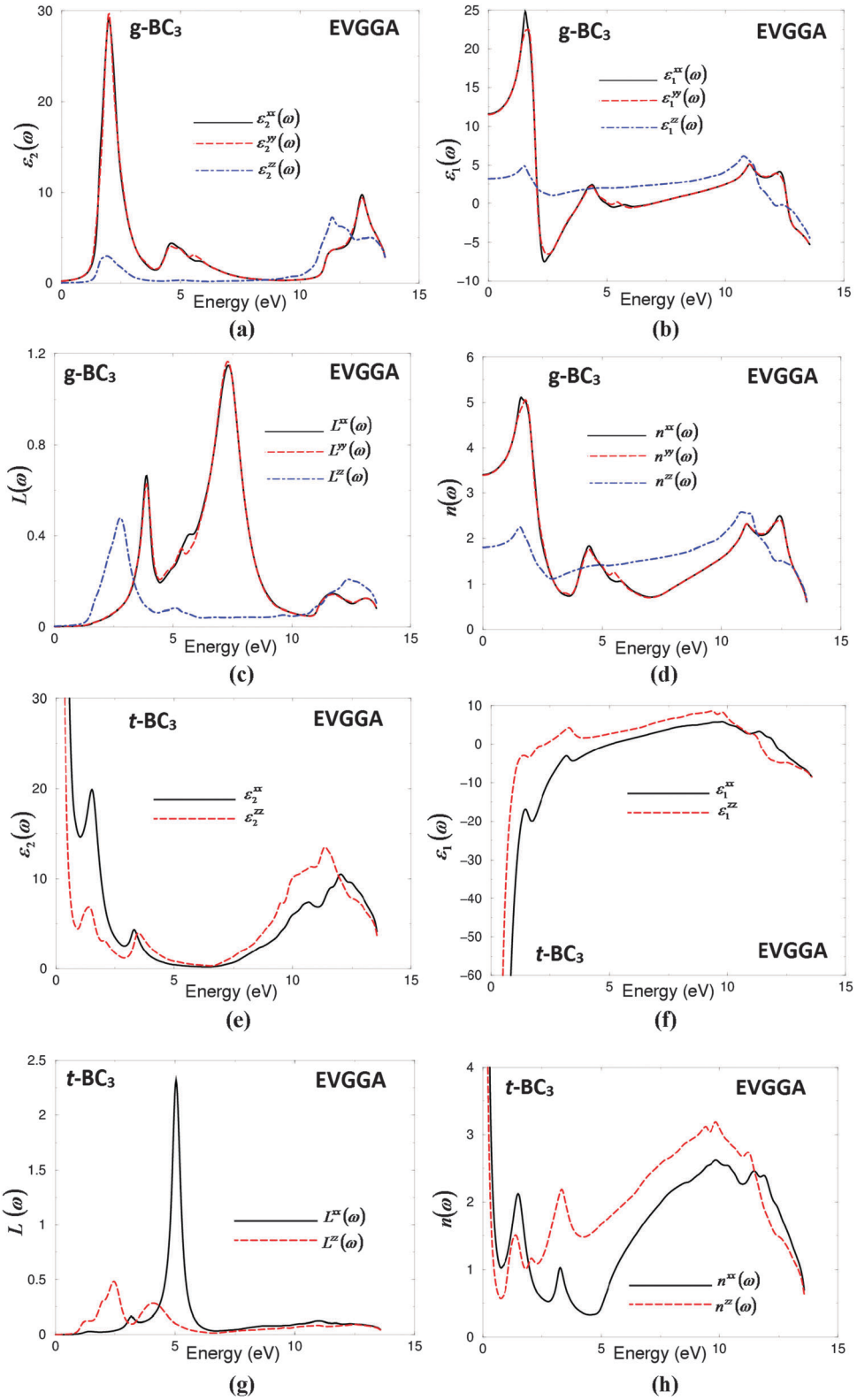

Fig. 9 (a) Calculated $\varepsilon_2^{xx}(\omega)$ (dark solid curve-black color online), $\varepsilon_2^{yy}(\omega)$ (light dashed curve-red color online) and $\varepsilon_2^{zz}(\omega)$ (light dotted dashed curve-blue color online); (b) calculated $\varepsilon_1^{xx}(\omega)$ (dark solid curve-black color online); $\varepsilon_1^{yy}(\omega)$ (light dashed curve-red color online) and $\varepsilon_1^{zz}(\omega)$ (light dotted dashed curve-blue color online); (c) calculated $L^{xx}(\omega)$ (dark solid curve-black color online), $L^{yy}(\omega)$ (light dashed curve-red color online) and $L^{zz}(\omega)$ (light dotted dashed curve-blue color online); (d) calculated $n^{xx}(\omega)$ (dark solid curve-black color online), $n^{yy}(\omega)$ (light dashed curve-red color online) and $n^{zz}(\omega)$ (light dotted dashed curve-blue color online); (e) calculated $\varepsilon_2^{xx}(\omega)$ (dark solid curve-black color online), and $\varepsilon_2^{zz}(\omega)$ (light dashed curve-blue color online); (f) calculated $\varepsilon_1^{xx}(\omega)$ (dark solid curve-black color online) and $\varepsilon_1^{zz}(\omega)$ (light dashed curve-blue color online); (g) calculated $L^{xx}(\omega)$ (dark solid curve-black color online) and $L^{zz}(\omega)$ (light dashed curve-blue color online); (h) calculated $n^{xx}(\omega)$ (dark solid curve-black color online), and $n^{zz}(\omega)$ (light dashed curve-blue color online).

and $\varepsilon_1^{zz}(\omega)$ of g-BC_3 phase are illustrated in Fig. 9(b), it confirms the existence of the strong high peak at around 2.0 eV, also it shows that $\varepsilon_1^{xx}(\omega)$ and $\varepsilon_1^{yy}(\omega)$ are isotropic and exhibit a strong anisotropy with $\varepsilon_1^{zz}(\omega)$ which is confirmed by the calculated values of $\varepsilon_1^{xx}(0) = \varepsilon_1^{yy}(0)$ about 11.5 and $\varepsilon_1^{zz}(0)$ of about 3.5. The uniaxial anisotropy $\delta\varepsilon = [(\varepsilon_0^{II} - \varepsilon_0^{\perp})/\varepsilon_0^{tot}] = -0.906$ indicating the existence of the considerable anisotropy between the parallel and the perpendicular polarization directions.

Fig. 9(a) and (b) shows that there are two absorption regions, the high absorption region occurs between 0.5 up to 5.0 eV and the low absorption region (10.0 eV up to 13.0 eV) where the crystal exhibits high transparency. The region confined between 5.0–10.0 eV is considered as a lossless region. Fig. 9(c) illustrates the loss function $L(\omega)$ which confirms the existence of the lossless region between 5.0 eV and 10.0 eV in coincidence with our observation in Fig. 9(a) and (b) and in agreement with previous work.[36] The loss function's peaks represent the plasma frequencies (ω_P). We should emphasize that above ω_P the material behaves as dielectric where $\varepsilon_1(\omega)$ is positive, while below ω_P where $\varepsilon_1(\omega)$ is negative the material exhibits metallic nature. In addition we have calculated the refractive indices of the g-BC_3 phase. The three tensor components of the refractive indices $n^{xx}(\omega)$, $n^{yy}(\omega)$ and $n^{zz}(\omega)$ are represented in Fig. 9(d). The two perpendicular ($n^{xx}(\omega)$ and $n^{yy}(\omega)$) components exhibit the highest refraction at around 2.0 eV in agreement with our previous findings (Fig. 9a and b) which confirm that this region is the high absorption region. Then the refractive indices decrease to reach their lowest value at energies around 14.0 eV (low absorption region). The values of the refractive indices at the static limit are 3.4 for $n^{xx}(0)$ and $n^{yy}(0)$, while it is 1.8 for $n^{zz}(0)$.

Fig. 9(e) represents the imaginary part of the optical dielectric functions $\varepsilon_2^{xx}(\omega)$ and $\varepsilon_2^{zz}(\omega)$ for the t-BC_3 phase. The sharp rise below 1.0 eV is attributed to the inclusion of the Drude term (intra -band transitions). It is due to the transitions between B-2p, C1,2,3-2p of the valence band and the three empty bands just above E_F (B-2p and C-2p of the CBC block and C-2p of the CCC block). Following Fig. 9(e) one can see the narrow lossless region (4.0–7.5) eV situated between the high and low absorption regions. The real part $\varepsilon_1^{xx}(\omega)$ and $\varepsilon_1^{zz}(\omega)$ (Fig. 9(f)) represents the intra-band transition (Drude term) below 1.0 eV and the lossless region between 4.0 and 7.5 eV. The loss function $L(\omega)$ of the t-BC_3 phase is illustrated in Fig. 9(g), which shows that the lossless region shift towards lower energies in comparison with the g-BC_3 phase (Fig. 9c). The refractive indices $n^{xx}(\omega)$ and $n^{zz}(\omega)$ of t-BC_3 are represented in Fig. 9(h). It shows the contribution of the intra -band transitions below 1.0 eV and the lossless region (4.0–7.5) eV. The optical properties of the t-BC_3 phase exhibit considerable anisotropy between the two optical components along the polarization directions [100] and [001]. Therefore, t-BC_3 is an optical anisotropic phase in agreement with previous calculations.[22] We should emphasize that the anisotropy in the linear optical susceptibilities favors an enhanced phase matching conditions necessary for observation of the second harmonic generation (SHG) and optical parametric oscillation (OPO).

3.4. Nonlinear optical response

Since the t-BC_3 phase is constructed by two different building blocks (CCC and CBC) to form sandwich-like layered structure with alternately stacking sequences of atomic planes C–C–B–C–C–C–B–C–C, it results in the loss of inversion symmetry which in turn gives a non-zero second harmonic generation. The linear optical properties of t-BC_3 exhibit a considerable anisotropy which in turn enhanced the phase matching conditions that are necessary for generating the second harmonic. The t-BC_3 phase crystallizes in tetragonal symmetry which allows only six nonzero tensor components, these are the complex second-order nonlinear optical susceptibility tensors $\chi_{123}^{(2)}(\omega) = \chi_{213}^{(2)}(\omega) = \chi_{132}^{(2)}(\omega) = \chi_{231}^{(2)}(\omega)$ and $\chi_{312}^{(2)}(\omega) = \chi_{321}^{(2)}(\omega)$, resulting in only two components $\chi_{123}^{(2)}(\omega)$ and $\chi_{321}^{(2)}(\omega)$. The formulae of complex second-order nonlinear optical susceptibility tensors are given in ref. 37–39. Fig. 10(a) illustrates $|\chi_{123}^{(2)}(\omega)|$ and $|\chi_{312}^{(2)}(\omega)|$, it is clear that $|\chi_{123}^{(2)}(\omega)|$ acts as the dominant component of about 3.5 pm V^{-1} at the static limit and 5.8 pm V^{-1} at λ = 1064 nm which suggest that the t-BC_3 single crystal could be as a promising nonlinear optical crystal in comparison with the experimental value of the well known $KTiOPO_4$ single crystal which exhibits a second harmonic generation (SHG) value of about 1.19 ± 0.08 pm V^{-1} (ref. 40) and 1.91 ± 0.2 pm V^{-1} (ref. 41) for the $|\chi_{113}^{(2)}(\omega)|$ component. The imaginary parts of the two components are calculated and presented in Fig. 10(b)

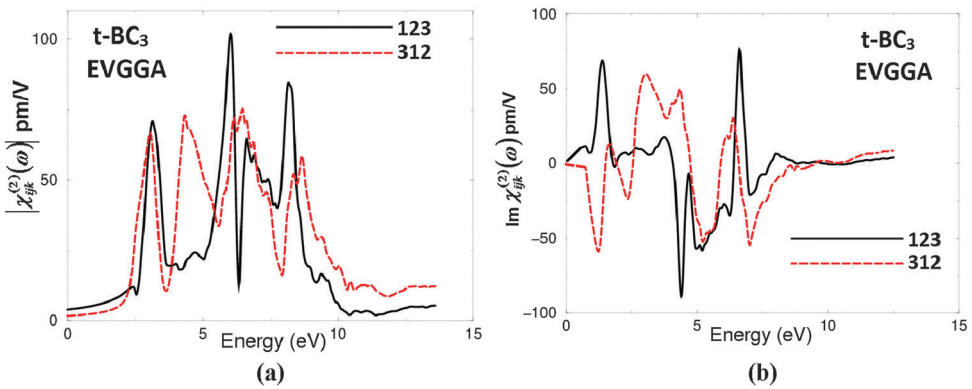

Fig. 10 (a) Calculated $|\chi_{123}^{(2)}(\omega)|$ (dark solid curve-black color online) and $|\chi_{321}^{(2)}(\omega)|$ (light long dashed curve-red color online) using EVGGA; (b) calculated $\mathrm{Im}\chi_{123}^{(2)}(\omega)$ (dark solid curve-black color online) and $\mathrm{Im}\chi_{321}^{(2)}(\omega)$ (light long dashed curve-red color online) using EVGGA.

which shows that both compounds oscillate around the zero along the whole energy range. We would like to mention here that in our previous studies[42–48] we have calculated the linear and nonlinear optical susceptibilities using the FPLAPW method on several systems whose linear and nonlinear optical susceptibilities are known experimentally, in those previous calculations we found very good agreement with the experimental data. Thus, we believe that our calculations reported in this paper would produce very accurate and reliable results.

4. Conclusions

Some specific features of electronic structures, linear and nonlinear optical susceptibilities of superhard g-BC_3 and t-BC_3 phases are investigated. We have employed the all-electron full potential linearized augmented plane wave within LDA, GGA and EVGGA. The calculated electronic band structure shows that the g-BC_3 phase is a semiconductor while the t-BC_3 phase is metallic. The calculated total and partial density of states confirm this finding and the values of the density of states at the Fermi level $N(E_F)$ and the electronic specific heat coefficient (γ) for the t-BC_3 phases are reported. Calculations show that both phases have only B–C and C–C bonds. The Fermi surface is formed by three empty orbitals. The electronic charge density confirms the existence of the two types of bonds (B–C and C–C). The linear and nonlinear optical responses are obtained based on the calculated band structure. The linear optical response exhibits a considerable anisotropy. The calculated SHG suggests that the t-BC_3 phase could be as a promising NLO crystal in comparison with the well known $KTiOPO_4$ single crystal.

Acknowledgements

The result was developed within the CENTEM project, reg. no. CZ.1.05/2.1.00/03.0088, cofunded by the ERDF as part of the Ministry of Education, Youth and Sports OP RDI programme and, in the follow-up sustainability stage, supported through CENTEM PLUS (LO1402) by financial means from the Ministry of Education, Youth and Sports under the "National Sustainability Programme I. Computational resources were provided by MetaCentrum (LM2010005) and CERIT-SC (CZ.1.05/3.2.00/08.0144) infrastructures.

References

1 E. A. Ekimov, V. A. Sidorov, E. D. Bauer, N. N. Mel'nik, N. J. Curro, J. D. Thompson and S. M. Stishov, *Nature*, 2004, **428**, 542.
2 P. V. Zinin, L. C. Ming, I. Kudryashov, N. Konishi and S. K. Sharma, *J. Raman Spectrosc.*, 2007, **38**, 1362.
3 V. L. Solozhenko, O. O. Kurakevych, D. Andrault, Y. Le Godec and M. Mezouar, *Phys. Rev. Lett.*, 2009, **102**, 015506.
4 V. L. Solozhenko, N. A. Dubrovinskaia and L. Dubrovinsky, *Appl. Phys. Lett.*, 2004, **85**, 1.
5 A. Champi and F. C. Marques, *Braz. J. Phys.*, 2006, **36**, 462.
6 F. J. Ribeiro and M. L. Cohen, *Phys. Rev. B: Condens. Matter Mater. Phys.*, 2004, **69**, 212507.
7 J. E. Moussa and M. L. Cohen, *Phys. Rev. B: Condens. Matter Mater. Phys.*, 2008, **77**, 8.
8 J. E. Lowther, *J. Phys.: Condens. Matter*, 2005, **17**, 3221.
9 H. Liu, Q. Li, L. Zhu and Y. Ma, *Phys. Lett. A*, 2011, **375**, 771–774.
10 P. V. Zinin, L. C. Ming, I. Kudryashov, N. Konishi and S. K. Sharma, *J. Raman Spectrosc.*, 2007, **38**, 1362.
11 Y. Ma, J. S. Tse, T. Cui, D. D. Klug, L. Zhang, Y. Xie, Y. Niu and G. Zou, *Phys. Rev. B: Condens. Matter Mater. Phys.*, 2005, **72**, 014306.
12 Y. Takano, T. Takenouchi, S. Ishii, S. Ueda, T. Okutsu, I. Sakaguchi, H. Umezawa, H. Kawarada and M. Tachiki, *Diamond Relat. Mater.*, 2007, **16**, 911.
13 K. W. Lee and W. E. Pickett, *Phys. Rev. Lett.*, 2004, **93**, 237003.
14 R. Hoffmann, T. Hughbanks, M. Kertesz and P. H. Bird, *J. Am. Chem. Soc.*, 1983, **105**, 4831.
15 C. J. Pickard, V. Milman and B. Winkler, *Diamond Relat. Mater.*, 2001, **10**, 2225.
16 J. L. He, L. C. Guo, E. Wu, X. G. Luo and Y. J. Tian, *J. Phys.: Condens. Matter.*, 2004, **16**, 8131.
17 M. M. Ali, A. K. M. A. Islam, M. Aftabuzzaman and F. Parvin, *J. Sci. Res.*, 2010, **2**, 203–213.
18 Z. Liu, J. He, J. Yang, X. Guo, H. Sun, H.-T. Wang, E. Wu and Y. Tian, *Phys. Rev. B: Condens. Matter Mater. Phys.*, 2006, **73**, 172101.
19 P. V. Zinin, L. C. Ming, S. K. Sharma, S. M. Hong, Y. Xie, T. Irifune and T. Shinmei, *J. Phys.: Conf. Ser.*, 2008, **121**, 062002.
20 D. Tomanek, R. M. Wentzcovitch, S. G. Louie and M. L. Cohen, *Phys. Rev. B: Condens. Matter Mater. Phys.*, 1988, **37**, 3134.
21 H. Sun, F. J. Ribeiro, J.-L. Li, D. Roundy, M. L. Cohen and S. G. Louie, *Phys. Rev. B: Condens. Matter Mater. Phys.*, 2004, **69**, 024110.
22 L. Li, W. Xue Li, D. Han, S. W. Xin, Y. Yang, W. Zhou and Y. Feng Lu, *Mater. Sci. Forum*, 2013, **749**, 551.
23 A. H. Reshak, *Phys. Chem. Chem. Phys.*, 2014, **16**, 10558.
24 G. E. Davydyuk, O. Y. Khyzhun, A. H. Reshak, H. Kamarudin, G. L. Myronchuk, S. P. Danylchuk, A. O. Fedorchuk, L. V. Piskach, M. Y. Mozolyuk and O. V. Parasyuk, *Phys. Chem. Chem. Phys.*, 2013, **15**, 6965.
25 A. H. Reshak, Y. M. Kogut, A. O. Fedorchuk, O. V. Zamuruyeva, G. L. Myronchuk, O. V. Parasyuk, H. Kamarudin, S. Auluck, K. J. Plucinskig and J. Bila, *Phys. Chem. Chem. Phys.*, 2013, **15**, 18979.
26 A. H. Reshak, D. Stys, S. Auluck and I. V. Kityk, *Phys. Chem. Chem. Phys.*, 2011, **13**, 2945.
27 P. Blaha, K. Schwarz, G. K. H. Madsen, D. Kvasnicka and J. Luitz, *WIEN2k, An augmented plane wave plus local orbitals program for calculating crystal properties*, Vienna University of Technology, Austria, 2001.
28 J. P. Perdew, S. Burke and M. Ernzerhof, *Phys. Rev. Lett.*, 1996, **77**, 3865.
29 W. Kohn and L. J. Sham, *Phys. Rev. A: At., Mol., Opt. Phys.*, 1965, **140**, 1133.

30 E. Engel and S. H. Vosko, *Phys. Rev. B: Condens. Matter Mater. Phys.*, 1993, **47**, 13164.
31 A BC_3 monolayer in an unrelaxed graphite structure with $d_{BC} = d_{CC} = 1.42$ Å is calculated to be an indirect-gap semiconductor with a negligibly small gap. This gap opens upon structural relaxation. In general, the true gap is larger than the calculated LDA gap, as discussed, *e.g.*, by M. S. Hybertsen and S. G. Louie, *Phys. Rev. B: Condens. Matter Mater. Phys.*, 1986, **34**, 5390.
32 F. M. Gao, J. L. He, E. Wu, S. M. Liu, D. L. Yu, D. C. Li, S. Y. Zhang and Y. J. Tian, *Phys. Rev. Lett.*, 2003, **91**, 015502.
33 F. Bassani and G. P. Parravicini, *Electronic States and Optical Transitions in Solids*, Pergamon Press Ltd, Oxford, 1975, pp. 149–154.
34 F. Wooten, *Optical properties of solids*, Academic Press, New York and London, 1972.
35 M. I. Kolinko, I. V. Kityk and A. S. Krochuk, *J. Phys. Chem.*, 1992, **53**, 1315–1320.
36 D. Jana, L.-C. Chen, C. W. Chen and K.-H. Chen, *ISRN Nanotechnol.*, 2011, 759838.
37 S. Sharma, J. K. Dewhurst and C. Ambrosch-Draxl, *Phys. Rev. B: Condens. Matter Mater. Phys.*, 2003, **67**, 165332.
38 A. H. Reshak, PhD thesis, Indian Institute of Technology-Rookee, India, 2005.
39 S. N. Rashkeev and W. R. L. Lambrecht, *Phys. Rev. B: Condens. Matter Mater. Phys.*, 2001, **63**, 165212.
40 L. K. Cheng, L. T. Cheng, J. Galperin, P. A. M. Hotsenpiller and J. D. Bierlein, *J. Cryst. Growth*, 1994, **137**, 107.
41 H. Vanherzeele and J. D. Bierlein, *Opt. Lett.*, 1992, **17**, 982.
42 A. H. Reshak, V. Kityk and S. Auluck, *J. Phys. Chem. B*, 2010, **114**, 16705–16712.
43 A. H. Reshak, S. Auluck and I. V. Kityk, *J. Solid State Chem.*, 2008, **181**, 789–795.
44 A. H. Reshak, S. Auluck and I. V. Kityk, *J. Phys.: Condens. Matter*, 2008, **20**, 145209.
45 A. H. Reshak, *J. Chem. Phys.*, 2006, **124**, 104707.
46 A. H. Reshak, *Eur. Phys. J. B*, 2005, **47**, 503–508.
47 A. H. Reshak, S. Auluck, D. Stys, I. V. Kityk, H. Kamarudin, J. Berdowski and Z. Tylczynskif, *J. Mater. Chem.*, 2011, **21**, 17219.
48 A. H. Reshak, M. Piasecki, S. Auluck, I. V. Kityk, R. Khenata, B. Andriyevsky, C. Cobet, N. Esser, A. Majchrowski, M. S'wirkowicz, R. Diduszko and W. Szyrski, *J. Phys. Chem. B*, 2009, **113**, 15237.

